

Wave Gradiometry in Two Dimensions

by Charles A. Langston

Abstract The spatial displacement gradient of a seismic wave is related to displacement and velocity through two spatial coefficients for any one dimension. One coefficient gives the relative change of wave geometrical spreading with distance and the other gives the horizontal slowness and its change with distance. The essential feature of spatial gradient analysis is a time-domain relation between three seismograms that yields information on the amplitude and phase behavior of a seismic wave. Filter theory is used to find these coefficients for data from 2D areal arrays of seismometers, termed gradiometers. A finite-difference star is used to compute the displacement gradient for irregularly shaped gradiometers, and a relation for the frequency-dependent error in the displacement gradient is obtained and applied to ensure accurate estimates. This kind of array analysis is useful for gradiometers at any distance from a source and yields a variety of time-domain and frequency-domain views of wave-amplitude changes and horizontal phase velocity estimates across the gradiometer. For example, time-dependent horizontal slowness and wave-azimuth plots are natural results of the analysis. These time-domain maps may be used in conjunction with time–distance and horizontal slowness–distance models to locate seismic sources or may be used directly to study earth structure. These methods are demonstrated by using data from a small-aperture (~ 40 m) seismic gradiometer.

Introduction

A companion article (Langston [2006], hereafter called article 1) presented a formalism for analyzing seismic data from dense linear arrays called spatial gradient analysis. Spatial gradient analysis is based on relating the spatial derivative of a generic wave model to the amplitude of the original wave and its time derivative through the chain rule of differential calculus. The coefficients of this relationship yield estimates of the relative change in geometrical spreading of the wave and its horizontal phase velocity. The analysis can be used on dense arrays of matched seismic instruments, termed gradiometers, to investigate important wave characteristics that can be directly related to wave propagation in a layered earth. Images of geometrical spreading changes and horizontal slowness as a function of time can be produced to analyze observed seismic wave fields and give additional data to interpretations of wave travel time or polarization.

In this article, I extend the theory of spatial gradient analysis to 2D arrays of seismometers arranged on a horizontal surface. Arrays of this type have been used for many years for passive recording of seismic events at all distance ranges (e.g., Bungum *et al.*, 1971; Abrahamson *et al.*, 1987; Vogfjord and Langston, 1990; Wagner, 1997). Standard array analyses are usually based on frequency/wavenumber decomposition of a plane wave field and often rely on beaming, stacking, correlation, and other smoothing operations to

process the data (e.g., Aki and Richards, 1980; Nawab *et al.*, 1985). Spatial gradient analysis, on the other hand, relies on the natural smoothing of wave fields from the physics of wavelength-dependent wave propagation and basic characteristics of a disturbance that obeys a wave equation. Results are based on a local determination of what is essentially the strain. Because smoothing (or averaging) only occurs on the choice of the test horizontal wavelength, results guarantee exposure of variations in the wave field.

Note that Cauwenberghs *et al.* (2001) and Stanacevic *et al.* (2002) used the spatial gradient of the acoustic wave field to design small directional acoustic sensors (hearing aids) to separate interfering speech. This inspiration for using the spatial gradient of the pressure field comes from research on insects that shows that insects can detect the direction of sound using sensor spacings (ears) that are two orders of magnitude smaller than the wavelength of sound being detected (Robert *et al.*, 1999; Miles and Sundermuth, 2000). The mathematical basis of the technique in acoustics is termed “gradient flow” and assumes an incident plane wave with a Taylor’s expansion of the gradient in terms of time derivatives of the incident wave. A small array of microphones can be built onto a silicon chip to use this concept.

The 2D treatment of the spatial gradient of seismic waves yields additional information of wave azimuth and azimuthal radiation pattern compared to the 1D case (article 1).

This technique should be useful in the wave-field decomposition of near-field strong-motion data from dense arrays and in fast source location estimates using separated small arrays in a region. The theory follows much of article 1 but with the computation of x and y spatial derivatives derived from a 2D finite-difference star consisting of five stations. In the ideal case of perfect Δx and Δy distance increments between stations, the finite-difference star is good to second-order accuracy in the increment. However, care is taken to compute the finite difference for a somewhat irregular pattern of seismic stations to determine the theoretical error of the gradient computation for typical field deployments. In addition to theoretical array computations to show various uses of the method, the technique will be demonstrated using a data set from a small five-element seismic array.

Spatial Gradient Theory for Two-Dimensional Arrays

A Cylindrical Wave with Radiation Pattern and Distance-Dependent Horizontal Slowness

It is convenient to assume a local geographical coordinate system in both Cartesian and cylindrical coordinates where the x and y axes are oriented east and north, respectively, and azimuth, θ , is measured clockwise from y to the radius vector, \vec{r} . Following article 1, I assume a propagating wave displacement of the form:

$$u(t, r, \theta) = G_r(r)R(\theta)f(t - p_r(r)(r - r_0)). \quad (1)$$

The radial and azimuthal derivatives are given by

$$\begin{aligned} \frac{\partial u(t, r, \theta)}{\partial r} &= A_r(r)u(t, r, \theta) + B_r(r) \frac{\partial u(t, r, \theta)}{\partial t} \\ \frac{\partial u(t, r, \theta)}{\partial \theta} &= \Re(\theta)u(t, r, \theta), \end{aligned} \quad (2)$$

where

$$A_r(r) = \frac{G'_r(r)}{G_r(r)} \quad (3)$$

$$B_r(r) = -\left[p_r + \frac{\partial p_r}{\partial r}(r - r_0)\right] \quad (4)$$

and

$$\Re(\theta) = \frac{R'(\theta)}{R(\theta)}. \quad (5)$$

The radial coefficients defined by equations (3) and (4) are of the same form as the Cartesian coefficients $A(x)$ and $B(x)$ defined in article 1. The addition of a radiation pattern term yields an additional coefficient (equation 5) that gives the relative change in radiation pattern with azimuth. As shown

in article 1, once these coefficients are found they may be integrated to obtain the geometrical spreading, horizontal slowness, and, now, the radiation pattern of the wave. Integrating equations (3) and (4) with radial distance gives

$$\int_{r_0}^r A_r(r)dr = \ln \frac{G_r(r)}{G_r(r_0)} \quad (6)$$

$$p_r(r) = -\frac{1}{(r - r_0)} \int_{r_0}^r B_r(r)dr. \quad (7)$$

Likewise, the radiation pattern is given by

$$\int_{\theta_0}^{\theta} \Re(\theta)d\theta = \ln \frac{R(\theta)}{R(\theta_0)}. \quad (8)$$

Although r and θ are part of a natural source coordinate system, the source position relative to an array is usually unknown and may even be the goal of the analysis. It is useful to relate the cylindrical displacement to a Cartesian form to solve for r and θ . Since

$$\begin{aligned} x &= r \sin \theta \\ y &= r \cos \theta \end{aligned} \quad (9)$$

the cylindrical derivatives can be written in terms of the Cartesian quantities as

$$\frac{\partial u}{\partial r} = \frac{\partial u}{\partial x} \sin \theta + \frac{\partial u}{\partial y} \cos \theta \quad (10)$$

$$\frac{1}{r} \frac{\partial u}{\partial \theta} = \frac{\partial u}{\partial x} \cos \theta - \frac{\partial u}{\partial y} \sin \theta. \quad (11)$$

Now assume the Cartesian form of the displacement as being

$$\begin{aligned} u(t, x, y) \\ = G(x, y)f(t - p_x(x - x_0) - p_y(y - y_0)) \end{aligned} \quad (12)$$

where the geometrical spreading and radiation pattern of the propagating wave is taken up in $G(x, y)$ and the horizontal slownesses, p_x and p_y , are components of the slowness vector in the x and y directions, respectively. Differentiating equation (12) gives

$$\frac{\partial u(t, x, y)}{\partial x} = A_x(x)u(t, x, y) + B_x(x) \frac{\partial u(t, x, y)}{\partial t} \quad (13)$$

$$\frac{\partial u(t, x, y)}{\partial y} = A_y(y)u(t, x, y) + B_y(y) \frac{\partial u(t, x, y)}{\partial t}.$$

Evaluating the derivatives of x and y in equation (10) gives

$$\theta = \tan^{-1} \frac{p_x}{p_y}. \quad (23)$$

$$A_r(r) = A_x(x)\sin \theta + A_y(y)\cos \theta \quad (14)$$

Finally, from equations (2) and (18)

$$B_r(r) = B_x(x)\sin \theta + B_y(y)\cos \theta \quad (15)$$

$$\frac{1}{r} \Re(\theta) = A_x(x)\cos \theta - A_y(y)\sin \theta. \quad (24)$$

where,

$$A_x(x) = \frac{1}{G(x,y)} \frac{\partial G(x,y)}{\partial x} \quad (16a)$$

$$A_y(y) = \frac{1}{G(x,y)} \frac{\partial G(x,y)}{\partial y} \quad (16b)$$

$$B_x(x) = -\left[p_x(x) + \frac{\partial p_x}{\partial x}(x - x_0)\right] \quad (17a)$$

$$B_y(y) = -\left[p_y(y) + \frac{\partial p_y}{\partial y}(y - y_0)\right]. \quad (17b)$$

Evaluating the derivatives for equation (11) gives

$$\begin{aligned} \frac{1}{r} \frac{\partial u}{\partial \theta} &= [A_x(x)\cos \theta - A_y(y)\sin \theta]u \\ &+ [B_x(x)\cos \theta - B_y(y)\sin \theta] \frac{\partial u}{\partial t}. \end{aligned} \quad (18)$$

By equations (2), this derivative cannot contain the velocity term (second term on the right hand side). Thus,

$$B_x(x)\cos \theta - B_y(y)\sin \theta = 0 \quad (19)$$

which can be solved to find the azimuth angle θ :

$$\theta = \tan^{-1} \frac{B_x(x)}{B_y(y)}. \quad (20)$$

This makes physical sense since, at a single point on the surface,

$$\begin{aligned} p_x &= -B_x(x_0) \\ p_y &= -B_y(y_0) \end{aligned} \quad (21)$$

$$p_r = p_x \sin \theta + p_y \cos \theta \quad (22)$$

and

In principle, a small gradiometer could be constructed to determine the two horizontal slownesses, both of which could be combined to find the radial slowness and azimuth using equations (22) and (23). If the array is large enough so that at least two independent estimates of the radiation pattern through the azimuthal derivative could be obtained for the same azimuth (using equation 24), then it appears possible to find the distance, r , from the source. For example, apply equation (24) at two different distances, say r_1 and r_2 , where $r_2 > r_1$ for corresponding Cartesian positions (x_1, y_1) and (x_2, y_2) . Then,

$$\frac{1}{r_1} \Re(\theta) = A_x(x_1)\cos \theta - A_y(y_1)\sin \theta \quad (25)$$

$$\frac{1}{r_2} \Re(\theta) = A_x(x_2)\cos \theta - A_y(y_2)\sin \theta. \quad (26)$$

Divide equation (25) by (26) to find

$$\frac{r_2}{r_1} = \frac{A_x(x_1)\cos \theta - A_y(y_1)\sin \theta}{A_x(x_2)\cos \theta - A_y(y_2)\sin \theta} = a. \quad (27)$$

Since $(r_2 - r_1)$ is known from the subarray positions and inferred azimuth, the distance of array 1 from the source is

$$r_1 = \frac{r_2 - r_1}{a - 1}. \quad (28)$$

This seems like a remarkable result because the radial geometrical spreading coefficient can have any functional form (as long as it's differentiable). However, the result is not too mysterious since it relies on the assumption that only one wave is propagating in the ideal way defined by equations (1) and (12). In practice, we would expect that the usual problems of anelasticity, wave scattering, and multiple wave interference could conspire to make solving for the distance difficult. However, this is an interesting result that might be feasible to use if an extended gradiometer were situated very close to a source and if the aperture of the gradiometer was of the same order of magnitude as the distance from the source.

Example 1. A Plane Wave

A typical assumption for most array analyses is that waves can be represented by plane waves. If the plane wave

is propagating in the direction of azimuth θ , with a constant horizontal slowness, p_0 , then

$$u(t, r, \theta) = f(t - p_0(r - r_0)) \quad (29)$$

or

$$u(t, x, y) = f(t - p_0 \sin \theta (x - x_0) - p_0 \cos \theta (y - y_0)). \quad (30)$$

Here,

$$G_r(r) = R(\theta) = 1 \quad (31)$$

so

$$A_x(x) = A_y(y) = \Re(\theta) = 0 \quad (32)$$

and

$$B_x(x) = -p_x = -p_0 \sin \theta \quad (33a)$$

$$B_y(y) = -p_y = -p_0 \cos \theta \quad (33b)$$

$$B_r(r) = -p_0 \quad (34)$$

$$\theta = \tan^{-1} \frac{B_x(x)}{B_y(y)}. \quad (35)$$

Example 2. A Surface Source with Radiation Pattern

This example includes both geometrical spreading and radiation pattern but with constant horizontal slowness. The cylindrical displacement is represented by

$$u(t, r, \theta) = \frac{\sin \theta}{r} f(t - p_0(r - r_0)) \quad (36)$$

where,

$$G_r(r) = \frac{1}{r} \quad (37)$$

and

$$R(\theta) = \sin \theta. \quad (38)$$

From equations (9) and (12)

$$\frac{\sin \theta}{r} = \frac{x}{x^2 + y^2} = G(x, y). \quad (39)$$

The Cartesian relative geometrical spreading coefficients are (by equation 16)

$$A_x(x) = \frac{y^2 - x^2}{x(x^2 + y^2)} \quad (40a)$$

$$A_y(y) = \frac{-2y}{x^2 + y^2}. \quad (40b)$$

Using equation (9) again with (40a, 40b)

$$\begin{aligned} A_r(r) &= A_x(x) \frac{x}{\sqrt{x^2 + y^2}} + A_y(y) \frac{y}{\sqrt{x^2 + y^2}} \\ &= -\frac{1}{\sqrt{x^2 + y^2}} = -\frac{1}{r}. \end{aligned} \quad (41)$$

Likewise, using equation (24) with (40a, 40b) gives

$$\Re(\theta) = yA_x(x) - xA_y(y) = \frac{y}{x} = \cot \theta. \quad (42)$$

The relations for horizontal slowness are the same as equations (33)–(35) in the plane-wave example.

Implementation of 2D Spatial Gradient Analysis

The strategy for applying this theory to the analysis of wave fields follows the results of article 1. An array of sensors distributed on a surface will be used to estimate the Cartesian spatial gradient of the wave field since the cylindrical coordinates (r, θ) are defined relative to an unknown source location. The Fourier transform of the spatial gradient equations will be used to find the Cartesian coefficients $A_x(x)$, $A_y(y)$, $B_x(x)$, and $B_y(y)$ following the results of article 1. These coefficients will be substituted into the preceding relationships to determine wave azimuth, slowness, $A_r(r)$, and $\Re(\theta)$. If the gradiometer is large enough, then other processing can be implemented, such as integrating $A_r(r)$ and $\Re(\theta)$ to recover the geometrical spreading and radiation pattern functions.

There are two major problems to overcome in the implementation. The first is to find accurate spatial derivatives of the wave field by using finite-difference relations for the gradiometer geometry. The second problem concerns the handling of displacement gradient/displacement spectral ratios to obtain accurate estimates of the Cartesian coefficients. An adequate solution to both problems must contain estimates of error. Computation of the spatial gradient requires that the wave field be filtered to avoid spatial aliasing of the derivatives. Interpretation of the spectral ratios to obtain the Cartesian coefficients requires the consideration of the variance of the estimates since the coefficients are theoretically constant, for some position, but the spectral ratio will be, in general, a changing function of frequency because of noise.

Solution for the Cartesian Coefficients

The solution for both the x and y Cartesian coefficients follows the results of linear array spatial gradient analysis presented in article 1. Fourier transforming the equations for the spatial derivatives yields

$$\hat{u}_{,x}(\omega, x, y) = A_x(x)\hat{u}(\omega, x, y) + i\omega B_x(x)\hat{u}(\omega, x, y) \quad (43a)$$

$$\hat{u}_{,y}(\omega, x, y) = A_y(y)\hat{u}(\omega, x, y) + i\omega B_y(y)\hat{u}(\omega, x, y). \quad (43b)$$

Dividing through by the transformed displacement gives (for example)

$$\frac{\hat{u}_{,x}(\omega, x, y)}{\hat{u}(\omega, x, y)} = A_x(x) + i\omega B_x(x). \quad (44)$$

Because the spatial coefficients are real

$$A_x(x) = \text{Re}\left\{\frac{\hat{u}_{,x}(\omega, x, y)}{\hat{u}(\omega, x, y)}\right\} \quad (45a)$$

$$A_y(y) = \text{Re}\left\{\frac{\hat{u}_{,y}(\omega, x, y)}{\hat{u}(\omega, x, y)}\right\} \quad (45b)$$

and

$$B_x(x) = \frac{1}{\omega} \text{Im}\left\{\frac{\hat{u}_{,x}(\omega, x, y)}{\hat{u}(\omega, x, y)}\right\} \quad (46a)$$

$$B_y(y) = \frac{1}{\omega} \text{Im}\left\{\frac{\hat{u}_{,y}(\omega, x, y)}{\hat{u}(\omega, x, y)}\right\}. \quad (46b)$$

Displacement gradient and displacement waveforms are windowed in the time domain and Fourier transformed to produce the spectral ratio. The mean value and variance of the real and imaginary parts of the spectral ratio are used to estimate the coefficients and their error, respectively, according to equations (45a, 45b) and (46a, 46b). As discussed in article 1, those values of the Cartesian coefficients are kept if the mean values are greater than two standard deviations of the estimate. This was called “variance filtering” in article 1 and deals with potential problems with noise, multiple wave arrivals, and other problems in taking a spectral ratio.

Computation of the 2D Displacement Gradient

Spatial gradient analysis is based on the relationship between three time series for a single point in space—the

displacement gradient, the displacement, and the velocity seismograms. It is necessary to take some care in making sure that the displacement gradient is computed for the same location as that for the displacement and velocity. In article 1, this was done using the central difference, which has second-order accuracy in the spatial increment. If a 2D array is constructed with exactly equal distance increments in x and y and receivers are all arranged at the corners of squares, then the x and y spatial derivatives and error estimates may be found independently using the 1D central difference adopted in article 1. A similar central difference star can be derived for a 2D arrangement of five seismometers (Fig. 1a) that is also of second-order accuracy in the distance increment (Abramowitz and Stegun, 1968). Keeping the third-order derivative as the error term (the second-order derivative drops out), the x and y spatial derivatives are given by

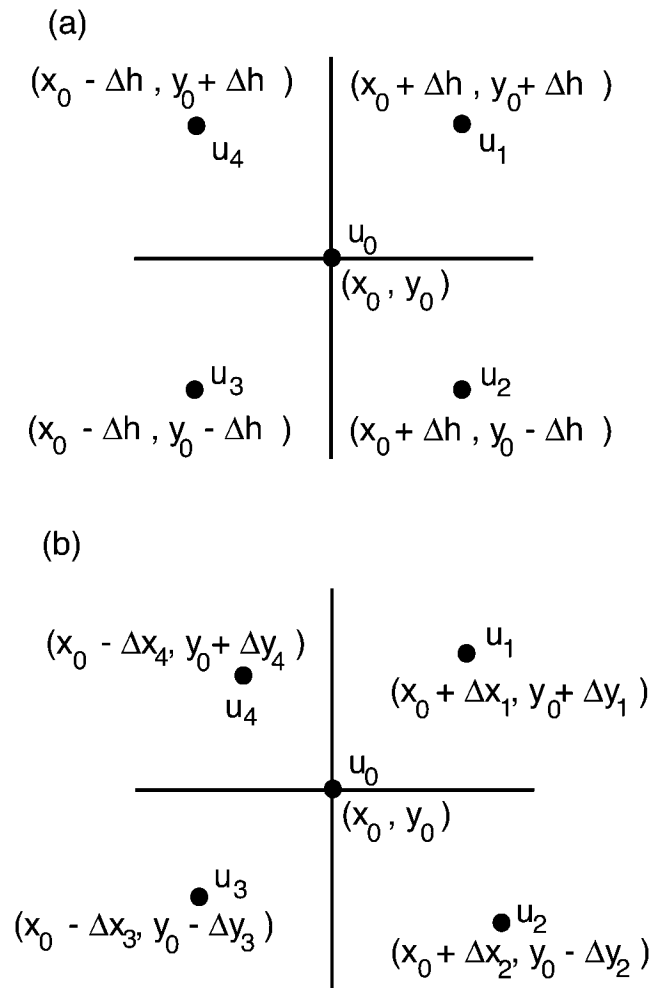


Figure 1. Two-dimensional finite-difference stars used to compute the horizontal derivatives. (a) A second-order accuracy star with equal increments, Δh , in x and y . (b) An imperfect difference star with irregular spacing between stations.

$$\left. \frac{\partial u}{\partial x} \right|_0 = \frac{1}{4\Delta x} \{u_1 + u_2 - u_3 - u_4\} - \frac{\Delta x^2}{6} \left. \frac{\partial^3 u}{\partial x^3} \right|_0 \quad (47a)$$

$$\left. \frac{\partial u}{\partial y} \right|_0 = \frac{1}{4\Delta y} \{u_1 + u_2 - u_3 + u_4\} - \frac{\Delta y^2}{6} \left. \frac{\partial^3 u}{\partial y^3} \right|_0. \quad (47b)$$

The individual error terms are identical with the 1D results (equation A3, article 1) which can be used to estimate the appropriate frequency band and horizontal wavenumber to avoid spatial aliasing when processing the data.

However, many 2D arrays are irregular because of logistical constraints in the field. It is practical to consider an irregular 2D array as shown in Figure 1b. This result will be used in a later section on data analysis. The object is to estimate the Cartesian spatial derivatives for point (x_0, y_0) using the values of displacement at all five points. Using the central point as the reference value in a Taylor's expansion, and letting

$$\Delta x_i = {}_x\varepsilon_i \Delta x \quad (48a)$$

$$\Delta y_i = {}_y\varepsilon_i \Delta y \quad (48b)$$

gives

$$\left. \frac{\partial u}{\partial x} \right|_0 = \frac{1}{\Delta x \sum_{i=1}^4 \frac{{}_x\varepsilon_i}{{}_y\varepsilon_i}} \left\{ \frac{u_1}{{}_y\varepsilon_1} + \frac{u_2}{{}_y\varepsilon_2} - \frac{u_3}{{}_y\varepsilon_3} - \frac{u_4}{{}_y\varepsilon_4} - \right. \quad (49a)$$

$$\left. u_0 \left[\frac{1}{{}_y\varepsilon_1} + \frac{1}{{}_y\varepsilon_2} - \frac{1}{{}_y\varepsilon_3} - \frac{1}{{}_y\varepsilon_4} \right] \right\} + \text{remainder} \left(\left. \frac{\partial u}{\partial x} \right|_0 \right)$$

$$\left. \frac{\partial u}{\partial y} \right|_0 = \frac{1}{\Delta y \sum_{i=1}^4 \frac{{}_y\varepsilon_i}{{}_x\varepsilon_i}} \left\{ \frac{u_1}{{}_x\varepsilon_1} - \frac{u_2}{{}_x\varepsilon_2} - \frac{u_3}{{}_x\varepsilon_3} + \frac{u_4}{{}_x\varepsilon_4} - \right. \quad (49b)$$

$$\left. u_0 \left[\frac{1}{{}_x\varepsilon_1} - \frac{1}{{}_x\varepsilon_2} - \frac{1}{{}_x\varepsilon_3} + \frac{1}{{}_x\varepsilon_4} \right] \right\} + \text{remainder} \left(\left. \frac{\partial u}{\partial y} \right|_0 \right).$$

The quantities ${}_x\varepsilon_i$ and ${}_y\varepsilon_i$ in equations (48a, 48b) and (49a, 49b) can be found by taking the mean of the absolute value of the Δx_i or Δy_i for an array geometry to obtain a value for Δx and Δy . The error of these finite-difference estimates for an irregular array become first-order in the distance increment rather than second-order as in the ideal finite-difference star (equation 47a, 47b). The remainder terms on the right-hand side of equation (49a, 49b) are, respectively,

$$\text{remainder} \left(\left. \frac{\partial u}{\partial x} \right|_0 \right) = \frac{1}{2 \sum_{i=1}^4 \frac{{}_x\varepsilon_i}{{}_y\varepsilon_i}} \left\{ \Delta x \left. \frac{\partial^2 u}{\partial x^2} \right|_0 \left(\frac{{}_x\varepsilon_1^2}{{}_y\varepsilon_1} + \frac{{}_x\varepsilon_2^2}{{}_y\varepsilon_2} - \frac{{}_x\varepsilon_3^2}{{}_y\varepsilon_3} - \frac{{}_x\varepsilon_4^2}{{}_y\varepsilon_4} \right) + \frac{\Delta y^2}{\Delta x} \left. \frac{\partial^2 u}{\partial y^2} \right|_0 ({}_y\varepsilon_1 + {}_y\varepsilon_2 - {}_y\varepsilon_3 - {}_y\varepsilon_4) \right\} \quad (50a)$$

$$\text{remainder} \left(\left. \frac{\partial u}{\partial y} \right|_0 \right) = \frac{1}{2 \sum_{i=1}^4 \frac{{}_y\varepsilon_i}{{}_x\varepsilon_i}} \left\{ \Delta y \left. \frac{\partial^2 u}{\partial y^2} \right|_0 \left(\frac{{}_y\varepsilon_1^2}{{}_x\varepsilon_1} - \frac{{}_y\varepsilon_2^2}{{}_x\varepsilon_2} - \frac{{}_y\varepsilon_3^2}{{}_x\varepsilon_3} - \frac{{}_y\varepsilon_4^2}{{}_x\varepsilon_4} \right) + \frac{\Delta x^2}{\Delta y} \left. \frac{\partial^2 u}{\partial x^2} \right|_0 ({}_x\varepsilon_1 - {}_x\varepsilon_2 - {}_x\varepsilon_3 + {}_x\varepsilon_4) \right\}. \quad (50b)$$

These remainder terms are useful for checking the accuracy of the spatial derivatives using the plane-wave assumption. For example, if the displacement is represented by

$$u(t, x, y) = e^{i\omega(t - p_x x - p_y y)} \quad (51)$$

the error is estimated by taking the first and second derivatives of equation (50a, 50b) and calculating, for example,

$$\delta = \frac{\text{remainder} \left(\left. \frac{\partial u}{\partial x} \right|_0 \right)}{\left. \frac{\partial u}{\partial x} \right|_0}. \quad (52)$$

Processing Data from 2D Arrays

A Synthetic Example for a Small Array

It is instructive to follow an ideal example of a propagating wave to investigate the behavior of the numerical spatial derivatives and one way to determine the error of the estimates of the radial spatial gradient coefficients. Similar to the example given in article 1, consider a cylindrical wave consisting of a Gaussian function time history, an assumed horizontal phase velocity, p_r , of 0.4 sec/km, geometrical spreading of r^{-1} and azimuthal radiation pattern of $\sin \theta$ (Fig. 2):

$$u(t, r, \theta) = \frac{\sin \theta}{r} e^{-100(t-1)^2} * \delta(t - p_r(r - r_0)) \quad (53)$$

Note that an arbitrary time shift of 1 sec has been included in the wave specification just for the purposes of display in Figure 2. Imagine that this wave is recorded by an ideal gradiometer of five sensors in the form of a square (Fig. 1a) with an increment, Δh , of 15 m. The center element is at $x = 2$ km, $y = 2$ km, and the source is located at $x = 0$ km, $y = 1$ km. The Cartesian spatial derivatives are computed

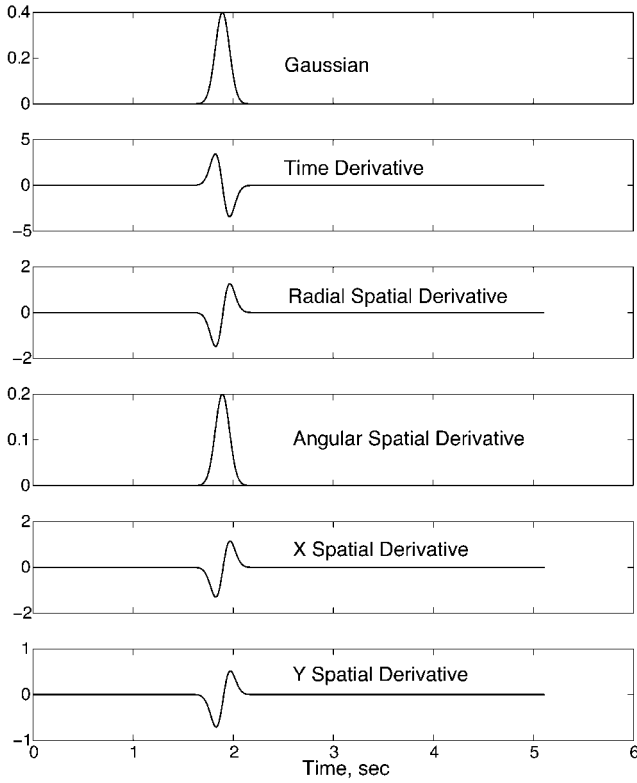


Figure 2. Numerical computation of the radial, angular, x , and y spatial derivatives of a Gaussian waveform (top panel) assuming a perfect finite-difference star (Fig. 1a) with an increment of 15 m. The Gaussian wave function is described by equation (53).

numerically using the finite-difference star in equation (47a, 47b) and are shown in the bottom two panels of the figure. The theoretical radial and azimuthal derivatives are also shown.

Figure 3 shows the results of performing the spatial gradient analysis on these wave forms using equations (44), (45a, 45b), and (46a, 46b) to obtain the Cartesian coefficients and equations (14), (15), and (24) to obtain the radial coefficients. Azimuth is found from equation (20). The plots show the coefficients as a function of frequency since they were obtained from the real and imaginary parts of the displacement gradient/displacement spectral ratio. The deviation of each coefficient from the true value is due entirely to the finite-difference approximation in computing the x and y derivatives of the displacement. The errors increase with frequency, as expected, but are uniformly small because the distance increment was chosen so that errors in the derivative would be 10% or less using the relation presented in article 1:

$$\Delta h \leq \lambda \frac{\sqrt{1.5\delta}}{\pi} = 0.123\lambda \quad (54)$$

where δ is the error (here 0.1) and λ is the wavelength.

The behavior of real data, however, has little to do with these ideal errors caused by discretization. Although it is important to design an array and filter the data to an appropriate frequency band to ensure the veracity of the gradient computation, noise, multiple wave arrivals, temporal aliasing, and other spectral complications often produce spectral ratios that show large variations across the frequency band. The approach suggested in article 1 was to calculate the mean value and variance of the spatial gradient coefficients over the frequency band of interest and then to only consider those estimated values that exceeded 2 standard deviations from zero. This was termed “variance filtering” and was essential in processing real array data.

Variance filtering is straightforward for linear arrays but the additional step of determining the radial spatial gradient coefficients and the azimuth through equations (14), (15), (24), and (20) requires that the errors found for A_x , A_y , B_x , and B_y be propagated correctly through the trigonometric relations involving azimuth. This is done numerically by using a Monte Carlo technique. Once the mean and variance of the Cartesian coefficients (e.g., for A_x , etc.) have been found from the Cartesian spectral ratios, 1000 artificial random errors each are generated from the observed variances for a standard distribution and used to find 1000 realizations of the radial coefficients and azimuth. The resulting frequency distributions are modeled as standard probability-density functions to determine the mean and variances of these radial coefficients and azimuth.

Figure 4 shows an example of this process to determine errors using the true values of the Cartesian parameters of the synthetic example (Fig. 3) but inflating the variance in B_x and B_y to 0.02 sec²/km² and 0.1 in A_x and A_y . The resulting probability-density functions are reasonably approximated by Gaussian distributions even with relatively large deviations in the azimuth.

Seismic Data from a Small Gradiometer

Data from a small experimental seismic/acoustic array are used as a proof of concept for 2D gradiometry. The array is located near the small town of Moscow, Tennessee, on private land and contains five surface elements arranged in a square (Fig. 5) and a central borehole approximately 10 m deep. Each surface element location has a three-component Mark Products L-28 short-period seismic sensor and an experimental infrasound microphone. There is a three-component L-28 sensor package at the bottom of the central borehole. The purpose of the array is to examine the interaction of atmospheric shock waves, specifically thunder, with near-surface soil structure. In addition to collecting a copious amount of thunderstorm events, the array has also recorded nearby earthquakes. The L-28 sensors are approximately flat to velocity between 2 and 25 Hz. They were calibrated before installation. Digital data are collected at a sampling rate of 200 samples/sec.

An event from the New Madrid Seismic Zone is pro-

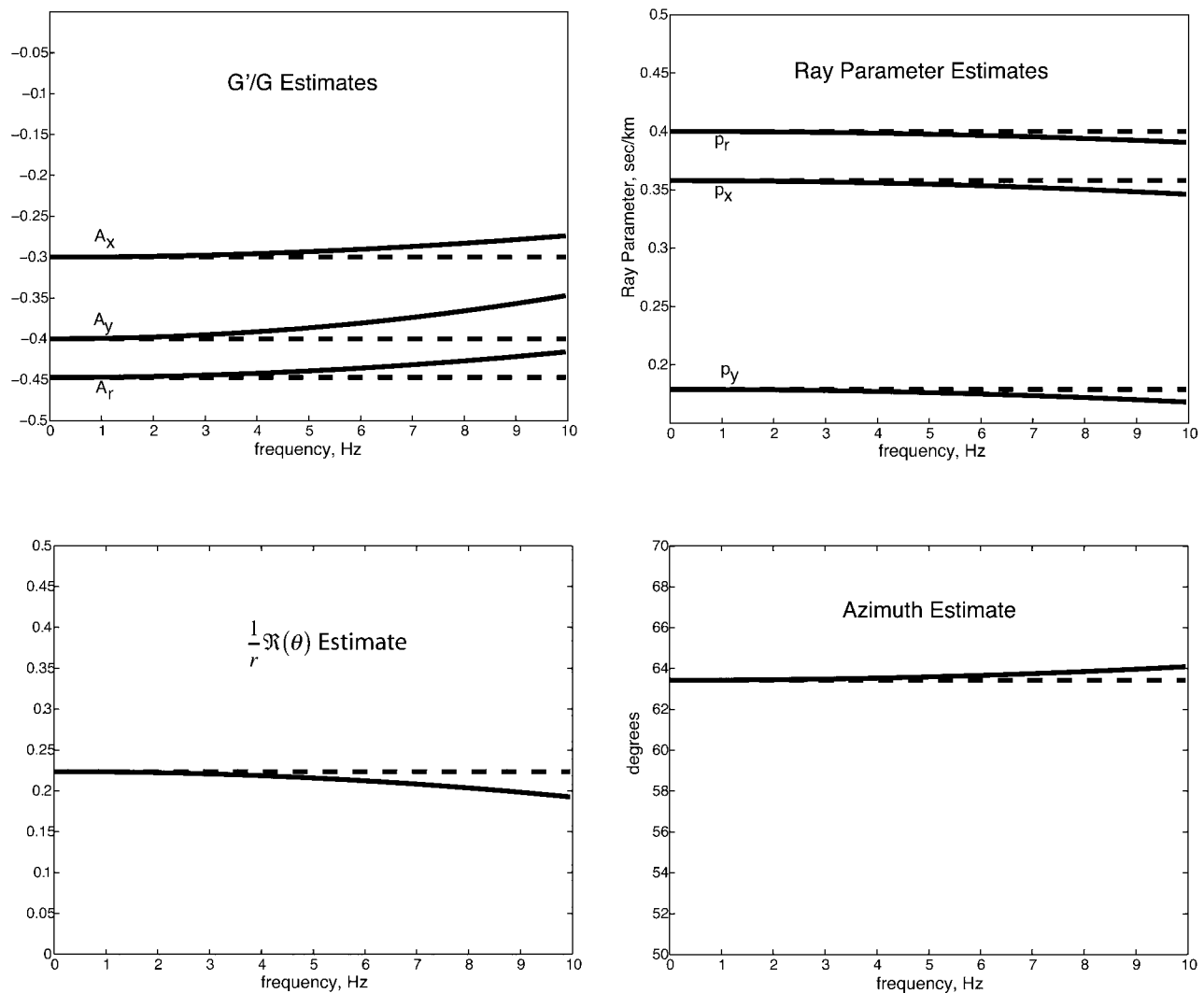


Figure 3. Gradiometry results using the numerical derivatives shown in Figure 2. The solid line for each coefficient or parameter is obtained from the spectral analysis and the dotted line denotes the true value. A_r is derived from A_x and A_y using equation (14). p_r is derived from p_x and p_y using equations (15) and (21). The radiation pattern change function is derived from equation (24) and the azimuth estimate from equation (20). The deviation from the true value is small in all cases and is due to the error in numerically computing the spatial partial derivatives.

cessed using the panoply of techniques presented previously and the moving window analysis presented in article 1. The data were bandpass filtered in four frequency bands with a two-pole phaseless Butterworth filter. Figure 6 shows the raw data from the surface sensors of the array and filtered records for the 3- to 4-Hz bandpass. Other bandpasses include 2–3, 4–5, and 5–6 Hz. The irregular finite-difference star, equation (49a, 49b), was used to compute the x (east–west) and y (north–south) spatial derivatives of the observed displacement seismograms using the surveyed locations of each surface element in the array. The spatial derivative waveforms and the central element waveform (element 5) were progressively windowed using a 10% cosine-tapered window 1 sec wide and shifted by 0.125 sec. Spatial gradient

analysis was performed after transforming the windowed time series into the frequency domain via fast Fourier transform (FFT) and the Monte Carlo technique used to estimate the variance and mean of the coefficient estimates.

Figure 7 shows the resulting determination of propagation azimuth and horizontal slowness that survived variance filtering for the 3- to 4-Hz bandpass. Waves should propagate in a direction of N173° at the gradiometer based on the excellent network location of the event. The inferred propagation azimuth is 167° ($\pm 2^\circ$) and 160° ($\pm 4^\circ$) for the P and S wave, respectively. Figure 8 is a summary of P - and S -wave azimuth and slowness determinations for the four bandpassed sets of seismograms. Also shown are estimates found by picking the arrival time of a prominent peak on

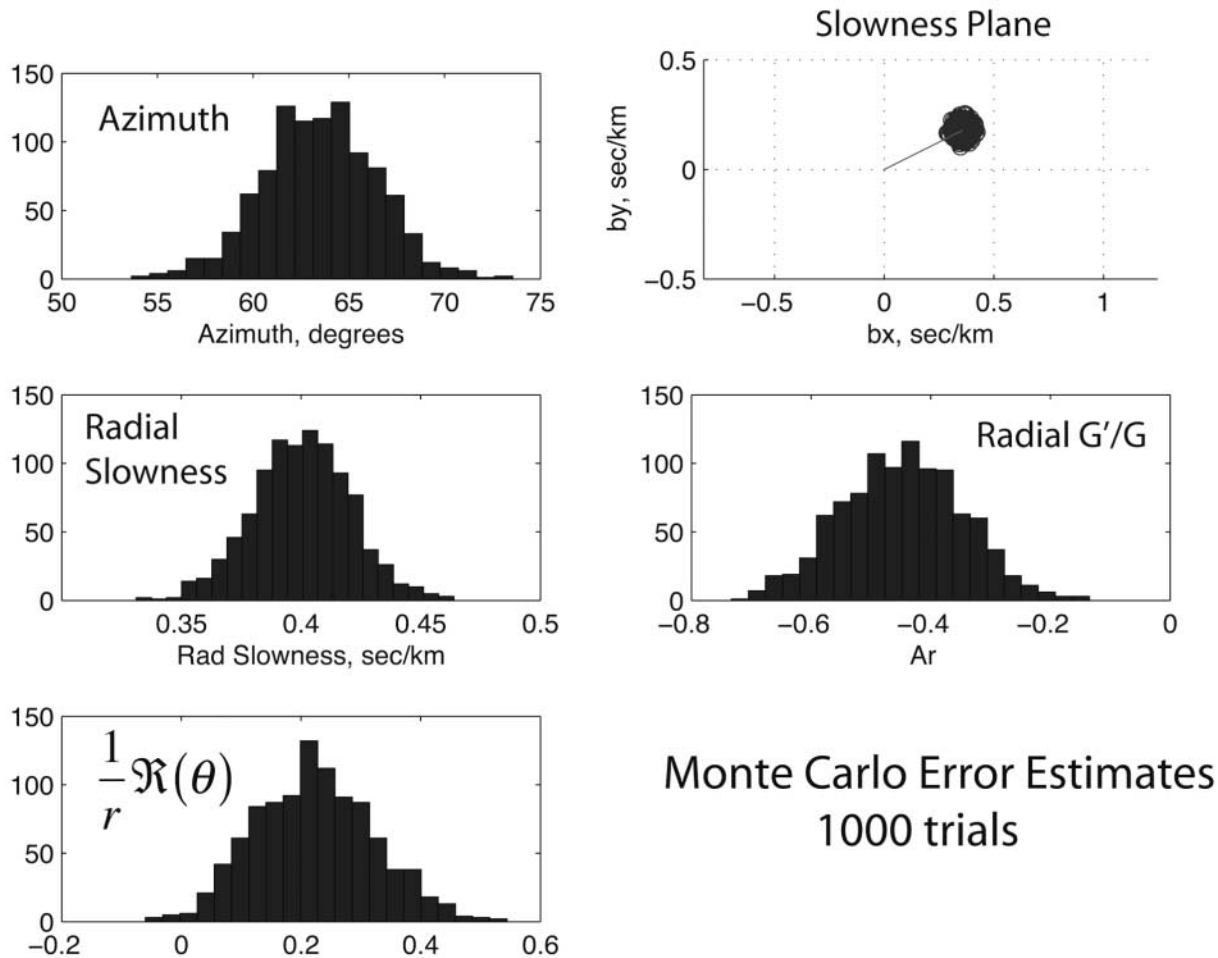


Figure 4. Numerical estimate of the errors in the radial coefficients of the synthetic wave SGA test shown in Figures 2 and 3 using artificially high standard deviations in the Cartesian coefficients (for the sake of display). A variance of 0.02 sec/km is assumed for the Cartesian estimates of slowness and a variance of 0.1 assumed for A_x and A_y . Some 1000 random perturbations were added to the Cartesian amplitude and slowness coefficients based on these assumed variances and the radial coefficients were computed using the equations in the text. The frequency distributions of the azimuth and radial coefficient determinations are adequately approximated by standard distributions and are shown in the various panels. The line on the slowness plane panel denotes the true value of radial slowness and azimuth.

both waves in the raw data and solving for p_x and p_y using the relative times between stations. Azimuth is the only unambiguous parameter known for this earthquake although it is likely that the apparent velocity for P should be 6.1–6.6 km/sec at this distance based on previous refraction measurements in the region (Mooney *et al.*, 1983). Likewise, the apparent velocity of S should be about 3.5–3.8 km/sec. Gradiometry estimates for azimuth are within 10° for data below 4 Hz and scatter to $\sim 25^\circ$ above 4 Hz. Error estimates are only about 2% in azimuth and 10% in apparent velocity. The parameter estimates for 3–4 Hz bandpassed data seem to give the best simultaneous estimates for P - and S -wave azimuths and slownesses, although the apparent velocities are a little low. Relative P - and S -wave velocities are nonphysical at 2–3 and 4–5 Hz since the S wave appears faster than P .

Note that there are numerous other single-wave detections within the seismograms with almost all having larger slowness (lower apparent velocity) and significantly different propagation azimuths. Figure 9 is a slowness scatter plot for the successful determinations in each frequency band. Most other detected waves within the P - and S -wave coda at 3–4 Hz appear to be forward-scattered surface waves within $\pm 45^\circ$ of the true event azimuth. The surface-wave interpretation comes from the very large slownesses observed that imply phase velocities as low as 250 m/sec. These low velocities are characteristic of surface waves within the unconsolidated sediments of the Mississippi embayment (Langston *et al.*, 2005). Figure 10 displays a histogram of the slowness detections of Figure 9. Forward scattering seems to dominate in the 2- to 3-Hz and 3- to 4-Hz

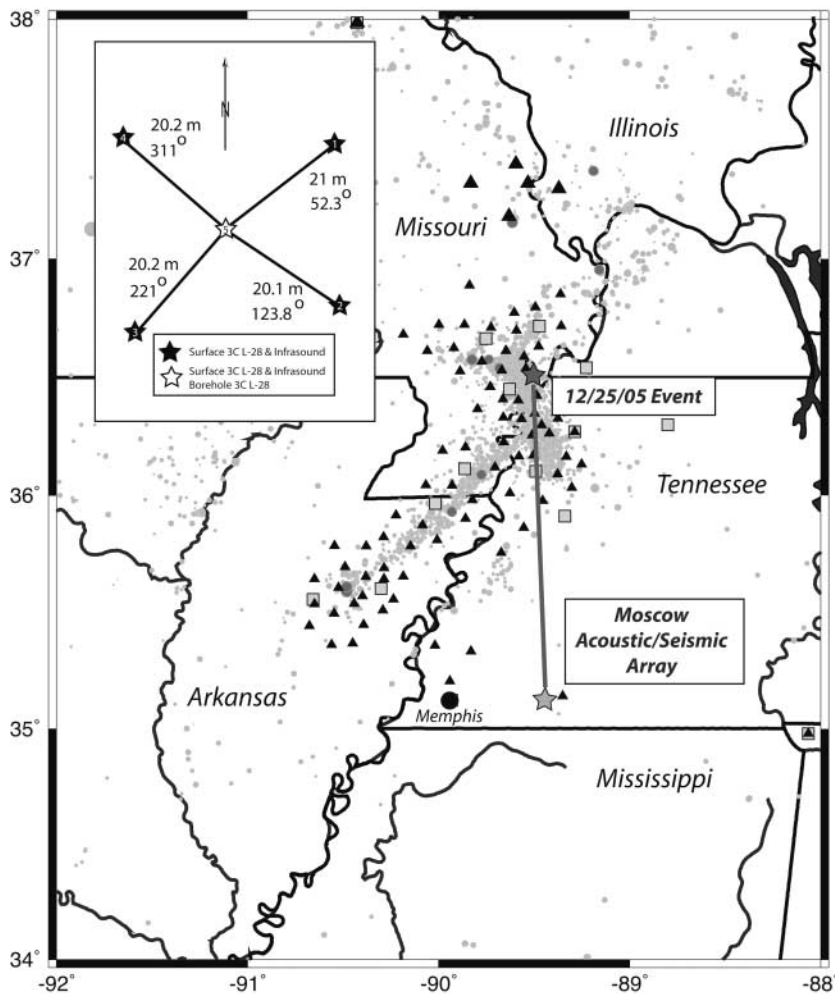


Figure 5. Index map showing the location of the New Madrid Seismic Zone (NMSZ), earthquakes are small gray circles, stations of the New Madrid Cooperative Network (squares and triangles), the location of the Moscow array (star), and the location of the 25 December 2005 M_d 2.8 earthquake (star) analyzed in subsequent figures. The event occurred at 14:33:45 UT at 36.53° N, 89.66° W at a depth of 12.4 km. The line shows the great circle path from the event to the array. Event distance is 161 km. The inset shows the geometry and physical specifications of the experimental array.

bands because most detections cluster around the true azimuth. However, scattering seems to be more isotropic with azimuth in the 4- to 5-Hz band. The 5- to 6-Hz results regain some directionality for the correct azimuth of propagation but also have significant amounts of backscattered waves.

Discussion

There are at least two ways of looking at the propositions of this article. On the one hand, 2D gradiometry offers an additional way to analyze the local characteristics of propagating wave fields to infer the direction and speeds of the waves. It may be an interesting alternative to standard array-processing techniques that rely on construction of beams, correlation, and frequency-wavenumber spectra to infer the same information. These standard techniques rely on observing distinct time shifts in highly correlated waveforms that propagate across the array and suffer when the correlation is degraded by earth structure heterogeneity. Modeling the spatial gradient can also suffer from structural heterogeneity because it is fundamentally a point measurement. It also requires highly correlated waveforms. Although correlation is virtually guaranteed because the measurement base-

line should be less than 10% of the wavelength (capitalizing on the natural physics of wave propagation) there can be numerous technical issues that make the measurement of small differences in a wave field very difficult. The caveats of article 1 in 1D spatial gradient analysis apply to 2D problems and are made somewhat more complicated because of the propagation of errors in performing two 1D problems to get the 2D result. These caveats include travel time and amplitude perturbations caused by earth structure heterogeneity, instrument calibration, and instrument installation. The error in computing the spatial gradient may be second-order in the array element spacing but is first-order in the amplitude measurement itself.

Nevertheless, gradiometry appears to be a viable method to efficiently study wave propagation over the duration of a complicated seismogram in a variety of wave-propagation regimes. As demonstrated with the Moscow array, gradiometry yields a picture of the composition of a seismogram that can be used to determine wave types through the propagation directions and speeds of those waves. This alone makes it a valuable seismological tool that could be used to solve general structural problems. A natural example is the propagation and reflection of strong-motion

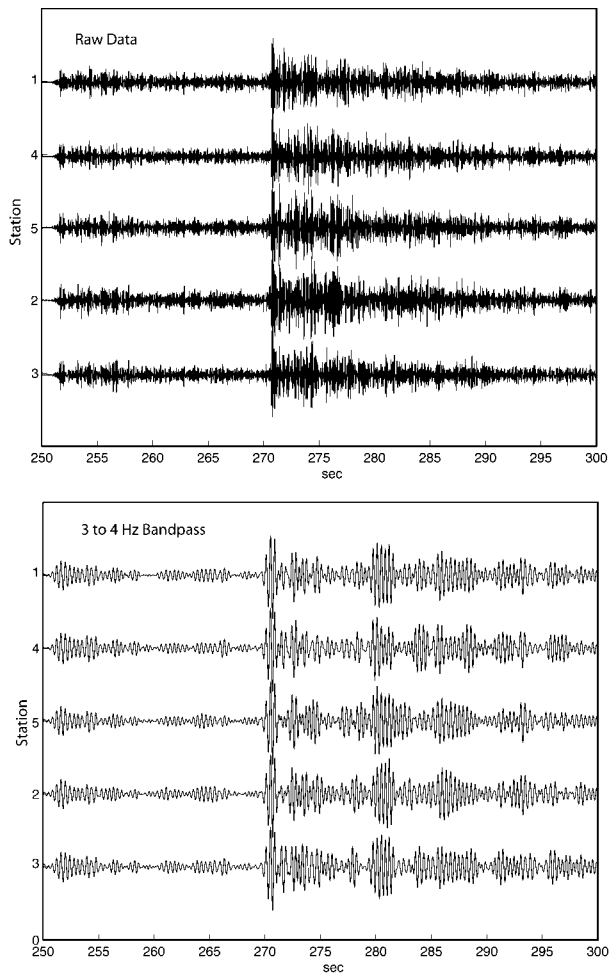


Figure 6. Vertical component seismic data recorded by the array (top panel). Also shown are data that have been bandpass filtered between 3 and 4 Hz (bottom panel).

surface waves within shallow sedimentary basins under urban areas (e.g., Bodin *et al.*, 1997).

On the other hand, one can run the technique in reverse, so to speak, by using it to investigate fine-scale variations in earth structure. Assuming that well-calibrated and well-installed instrumentation can be deployed, a large dense 2D wave gradiometer can be used to investigate the variations of amplitude and wave slowness across an area to infer fine-scale earth structure. Slowness, azimuth, geometrical spreading, and azimuthal changes of waves from controlled sources could be used in conjunction with accurate wave-propagation codes to infer quantitative estimates of structure. Alternatively, maps of these wave characteristics could be used in an empirical way to detect anomalous structure from controlled or natural sources that could then be used as a guide to perform more detailed investigations with other techniques (e.g., seismic refraction, etc.).

Applying these techniques to the Moscow array data illuminates several issues in data analysis and interpretation.

Real seismic wave fields are products of frequency-dependent scattering from 1D, 2D, and 3D structures in the earth. Seismic waves are only approximately represented by an equation such as (1) and the interpretation of a result obtained using any array technique always depends on how well the data agree with the original assumptions of the technique. Frequency–wavenumber techniques, for example, usually assume plane-wave propagation and rely on highly correlated waveforms recorded at all sensors in the array. The theory outlined here and in article 1 relies on an approximate and ideal representation of the seismic wave. As in beamforming, interfering waves can be separated if they have different wavenumber characteristics even if they arrive at the same time, that is, data can be filtered to separate waves if they have differing spectral content before applying the spatial gradient analysis (article 1).

Notably, I found that narrow bandpass filtering the data from the Moscow array was necessary to obtain azimuth and slowness estimates that passed the spectral ratio variance test. Using data over the entire frequency band of 2–6 Hz did not yield any significant result and suggested that even individual seismic waves, like *P* or *S*, are much more complex than is commonly assumed. In addition, the idea of a time or amplitude “static correction” due to site structure for an individual seismic station loses meaning in gradiometry because the technique implicitly uses the natural “smoothing” of frequency-dependent wave propagation. This is reflected in the results of Figure 8 that shows changing apparent velocities and azimuths as a function of frequency band. Probably the least relevant measurements of Figure 8 are those based on arrival times of the phases because relative times were of the order of the sampling rate of the seismograms. Nevertheless, it is likely that these results are due to the heterogeneity of the array site in a complicated way. Near-surface refraction measurements yield a *P*-wave velocity of 550 m/sec and an *S*-wave velocity of 320 m/sec (Ting-Li Lin, personal comm., 2006). These materials overlie nearly a kilometer of unconsolidated Mississippi embayment sediments with average *P* and *S* velocities of 1.8 km/sec and 0.6 km/sec, respectively. Lateral variations in these velocities are a certainty and the filtered data of Figure 6 clearly show significant variations in the waveform coda over the 20- to 40-m separation in array stations. Wave gradiometry offers a way to quantify the variations of a wave field that can then be used to understand the underlying variations in earth structure unlike standard beamforming array methods that average through these variations.

Another natural use of 2D gradiometry in seismology is in the investigation of earthquake source rupture kinematics. A large wave gradiometer could be constructed in a region of expected faulting during a large earthquake (e.g., southern California) and used to examine the kinematics of seismic-wave generation by the earthquake as a function of time and space. A useful characteristic of the theory presented here is that the source can be situated very close to

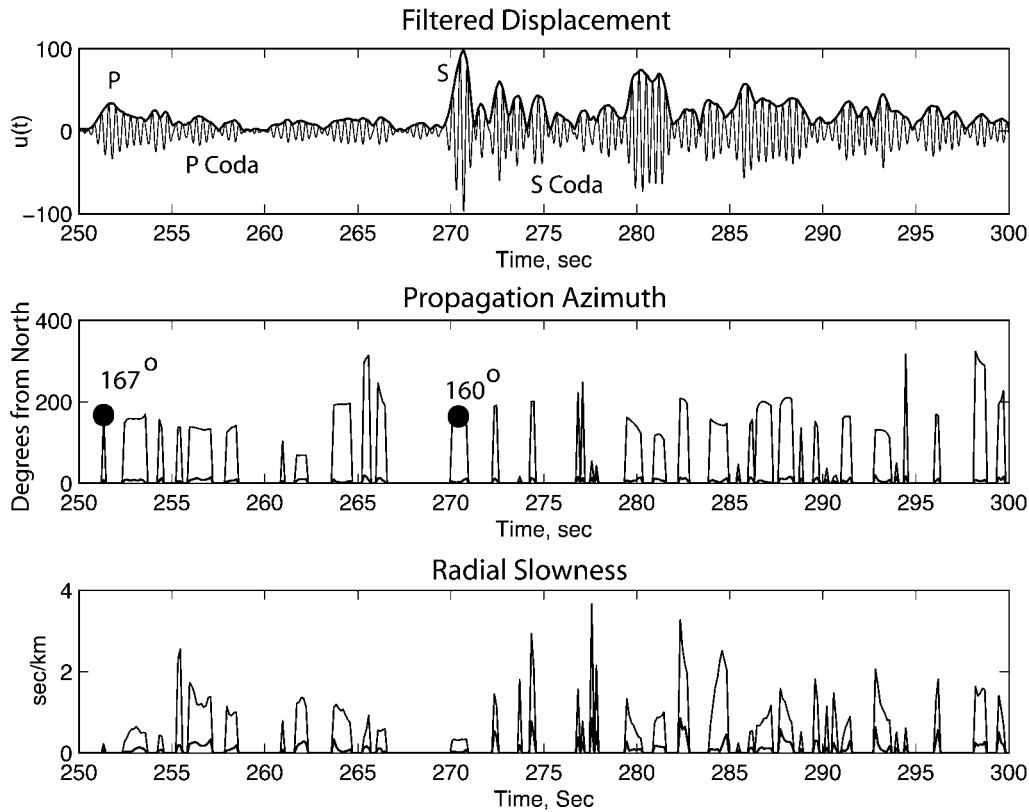


Figure 7. Moving window spatial gradient analysis of the data shown in Figure 6. The plane-wave model was assumed for the analysis. The top panel shows the filtered displacement waveform for the center element of the array with annotations for the *P* and *S* phases and regions of *P* and *S* coda. The middle panel shows the inferred wave-propagation azimuth after variance filtering. The inferred azimuths of the *P* and *S* phases are shown as filled circles. The bottom panel shows the inferred radial slowness. The value of 2 standard deviations in the estimates is shown as the gray line plotting near the time axis under the inferred azimuth and slowness values.

or even within the gradiometer. Wave-propagation directions and amplitude characteristics could be used in what essentially would be a dynamic location process to examine seismic-wave radiation from different parts of the fault.

A wave gradiometer would be composed of numerous seismic sensors placed in a regular lattice based on an appropriate finite-difference star to ensure regularity in the gradient computation. Note one technical detail for such arrays. Different economies for building a gradiometer can be obtained for covering an area. Figure 11 shows two situations where the array lattice is based on finite-difference stars that have the same second-order accuracy in the derivatives and the same spatial increment. The top array needs 59 seismic instruments to blanket the area but the bottom array only needs 32 instruments. Although the top array will have a denser coverage of the area, the bottom array should have the same performance in terms of accuracy of the gradients. The top array might be more appropriate for fine-scale structure studies within the array, but the bottom array could be sufficient for source studies. The bottom gradiometer would be about half the price of the top considering instrument and deployment costs.

There is nothing that stops application of gradiometry for three spatial dimensions. In its simplest form, a plane wave can be represented by

$$u(x, y, z, t) = f(t - p_x(x - x_0) - p_y(y - y_0) - p_z(z - z_0)). \quad (55)$$

Differentiation of this equation in all three coordinates yields three 1D sets of coefficients to determine the slowness vector. Inclusion of geometrical spreading and/or radiation pattern yields the same sorts of relations as presented here for two dimensions. An appropriate 3D wave gradiometer would be instruments situated in a body-centered cube arrangement (instruments at the corners and one in the center). This arrangement is a natural second-order difference star for computing the wave gradients in each dimension. A 3D seismic gradiometer could be built using fairly shallow boreholes in uniform geological materials. Other wave fields may be more conducive to 3D wave gradiometry in terms of ease of technical deployments. For example, it should be feasible to construct a compact body-centered cubic gradiometer for

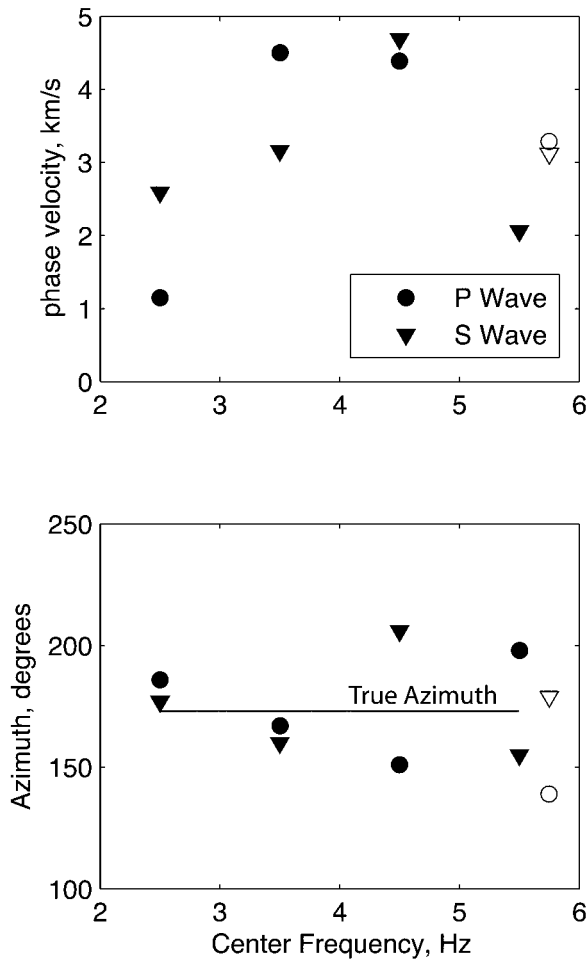


Figure 8. Summary of phase-velocity measurements (top panel) and azimuth measurements (bottom panel). The open symbols are determinations made by modeling high-resolution arrival times of major peaks in the *P* and *S* wave across the array. The mid-point of the passband used in the analysis has been assumed for plotting each gradiometry value (filled symbols).

atmospheric infrasound or for oceanic acoustic recording. An infrasound gradiometer built to analyze 10 Hz and lower frequency waves need only be 8 m or less on a side.

The lower limit to sensor spacing depends on the accuracy of instrument calibration. It is unlikely, in practice, to expect sensors to be calibrated better than 1% in amplitude across their primary frequency band. The limit for finding the difference in amplitude between two sensors would be where the error in amplitude measurement is equal to the change in amplitude of the wave over a distance of $2\Delta h$ for second-order accuracy. If this is modeled by a cos function, a 1% change in amplitude over $2\Delta h$ occurs for about a 2.3% change in wavelength. Thus, the difference increment, Δh , between gradiometer sensors should be greater than 1% of the wavelength for a second-order system. Combining this result with the second-order accuracy estimate given by

equation (54), the limits of typical gradiometers containing instruments calibrated to 1% should be

$$0.123\lambda_{\min} \geq \Delta h \geq 0.012\lambda_{\max} \quad (56)$$

where λ_{\min} is the minimum horizontal wavelength and λ_{\max} is the maximum horizontal wavelength. Thus, there is a theoretical horizontal bandwidth of about one decade for these kinds of gradiometers. Improvements should be possible in extending the horizontal bandwidths by gradiometer calibration through empirical controlled source experiments or electronic means. For example, a seismic gradiometer might be calibrated by modeling the response of a controlled source situated at different points outside of the array.

Wave gradiometry opens a new avenue of research and data collection efforts that should find use in quantifying numerous effects of wave propagation from wave sources of all types including seismic, acoustic, and electromagnetic wave fields. There are numerous variations on the theme of gradiometry that include the effects of filtering, velocity reduction, and analysis of anelastic attenuation for single propagating seismic waves (article 1). Indeed, there remain another class of problems involving discrimination of interfering signals that gradiometry can be applied to (e.g., Stanacevic *et al.*, 2002). Thus, the theory and techniques discussed in this article and article 1 are only a beginning for further theoretical developments and a platform for practical field experiments and instrumentation development for wave gradiometry.

Conclusions

The spatial gradient of a seismic-wave propagating in two dimensions is utilized to determine amplitude and phase characteristics of the wave that include horizontal slowness, direction of propagation, radial geometrical spreading changes, and azimuthal radiation pattern changes. The mathematical underpinning is based on the form of a generic seismic wave and relating its spatial derivatives to the original displacement and particle velocity. A 2D wave gradiometer is constructed theoretically by forming a surface finite-difference star to compute the Cartesian displacement gradients. Two 1D problems are performed to determine the response of a 2D wave gradiometer. The errors in determining the slowness, geometrical spreading, and radiation pattern coefficients are propagated through the equations using an empirical Monte Carlo technique.

These techniques were tested using data from a small, slightly irregular experimental seismic array with an aperture of only 40 m. Spatial gradient analysis wave form data from a local earthquake was successful in extracting the azimuth of propagation from the *P* and *S* wave and demonstrated that much of the waveform probably consisted of low-phase velocity forward- and backscattered surface waves.

Two-dimensional and even 3D wave gradiometry should be useful in analyzing seismic, acoustic, and electro-

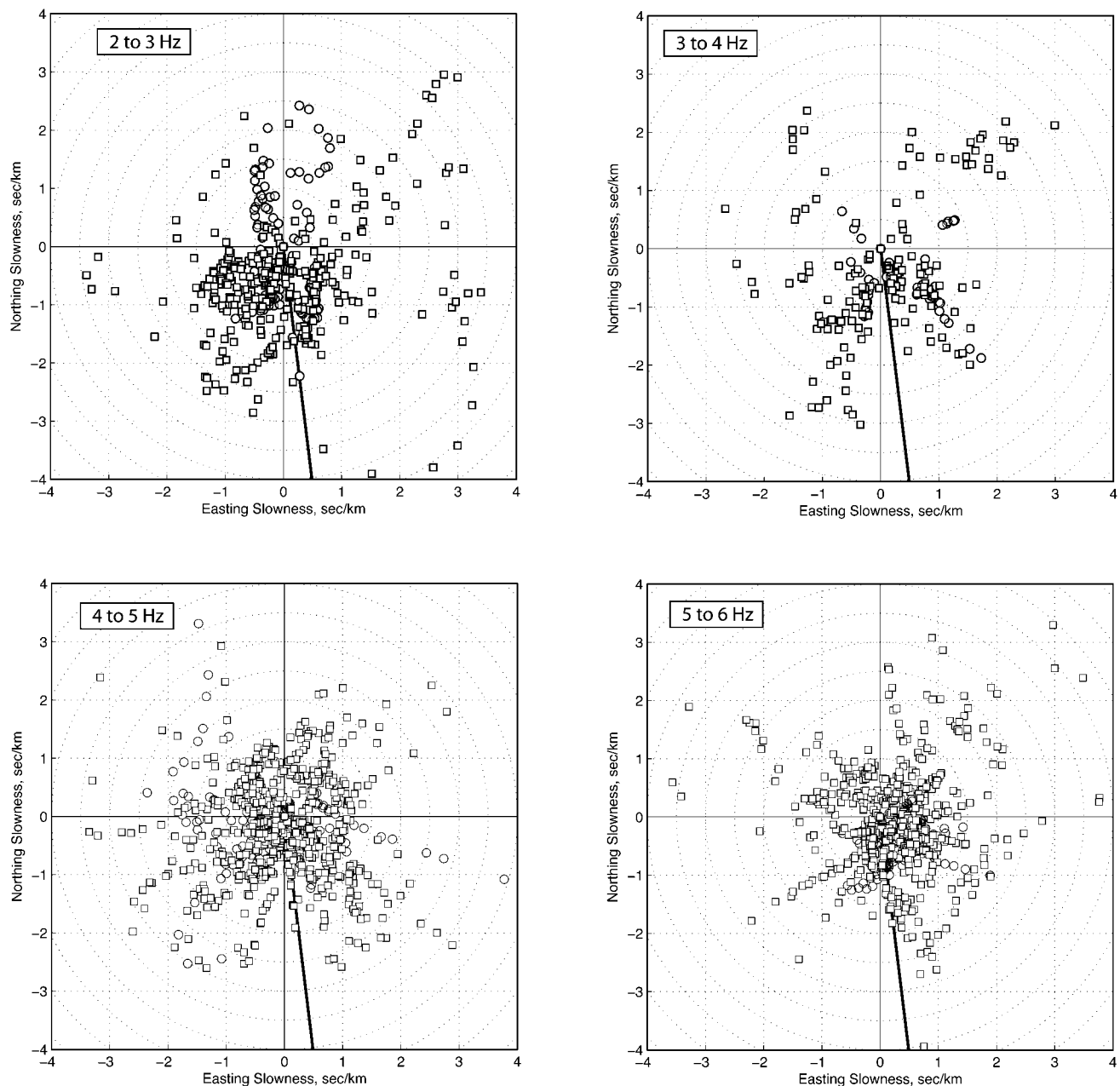


Figure 9. Scatter plots of the values of slowness on the wave slowness plane for the spatial gradient analysis performed in each passband. Each dot represents the location of radial slowness and azimuth determined from 50 sec of the vertical waveform of the 25 December 2005 event recorded at the Moscow array. The solid line is the azimuth based on the earthquake location and assuming wave propagation in a vertically inhomogeneous earth. Note how the slowness values are relatively large and distribute themselves differently according to the frequency band assumed. A small percentage of slowness directions actually occur in the expected azimuth.

magnetic wave fields to determine source parameters as well as characteristics of the structure within the gradiometer.

Acknowledgments

This work was supported by the Mid America Earthquake Center through contracts HD-3 and HD-5. Bob Smalley read the first draft of this manuscript and made several useful suggestions for its improvement. I also

thank reviewers Paul Spudich and Cinna Lomnitz for many useful comments that further improved the manuscript. This is CERI contribution number 508.

References

- Abrahamson, N. A., B. A. Bolt, R. B. Darragh, J. Penzien, and Y. B. Tsai (1987). The SMART-I accelerograph array (1980–1987): a review, *Earthquake Spectra* **3**, 263–287.

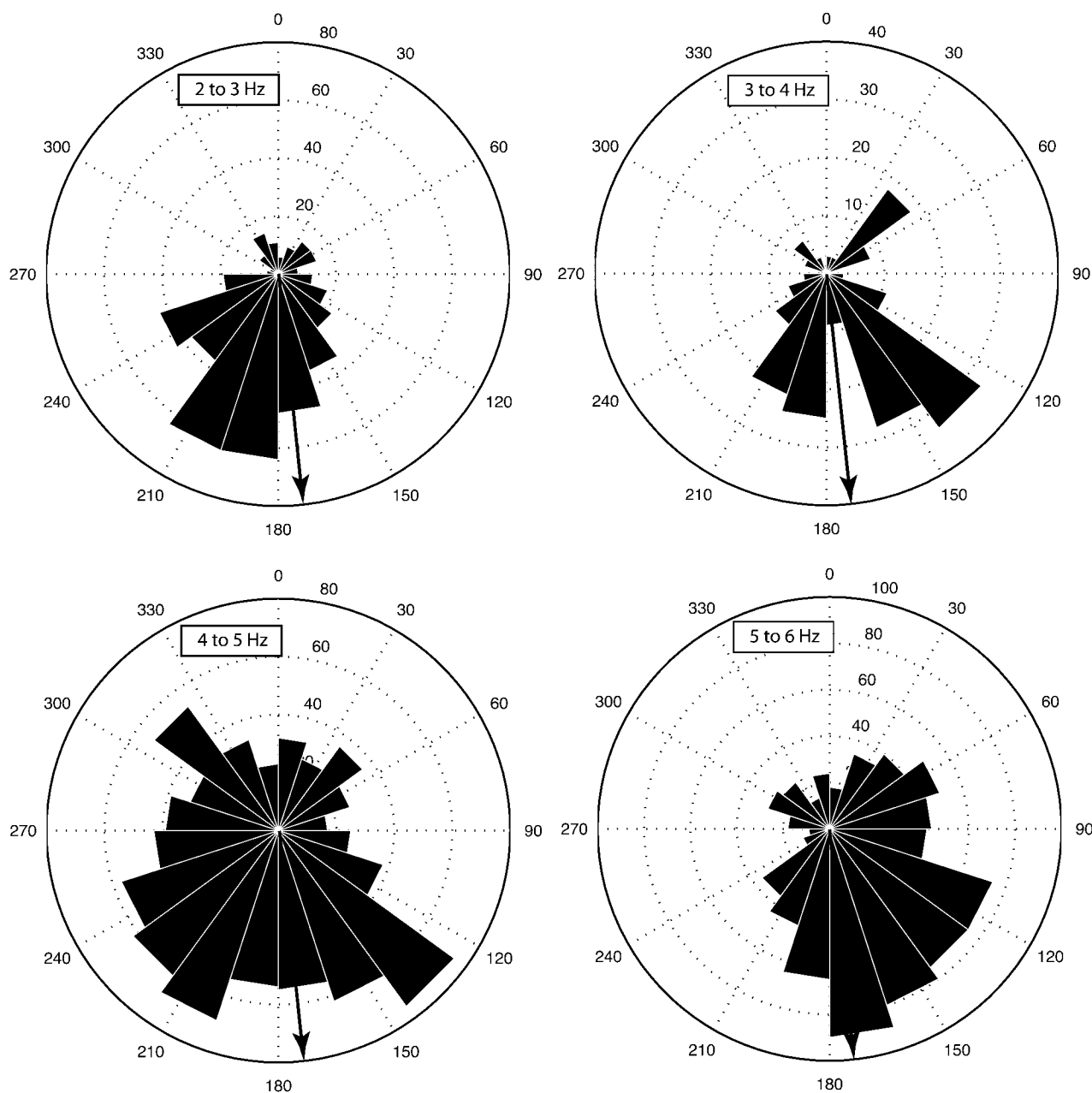


Figure 10. A histogram of the number of slowness values in 10 deg bins of azimuth using the data of Figure 9. The arrow denotes the ideal wave-propagation azimuth. Arrivals generally cluster in several directions within 45° of the expected azimuth except for the data in the 4- to 5-Hz band. Here it appears that scattering is much more isotropic including a significant proportion of backscattered waves.

- Abramowitz, M., and I. A. Stegun (1968). *Handbook of Mathematical Functions*, Dover Publications, New York.
- Aki, K., and P. G. Richards (1980). *Quantitative Seismology: Theory and Methods*, W. H. Freeman and Co., San Francisco, California.
- Bodin, P., J. Gomberg, S. K. Singh, and M. Santoyo (1997). Dynamic deformation of shallow sediments in the Valley of Mexico, Part I: Three-dimensional strains and rotations recorded on a seismic array, *Bull. Seism. Soc. Am.* **87**, 528–539.
- Bungum, H., E. S. Huseby, and F. Ringdal (1971). The NORSAR array and preliminary results of data analysis, *Geophys. J. R. Astr. Soc.* **25**, 115–126.

- Cauwenberghs, G., M. Stanacevic, and G. Zweig (2001). Gradient flow broadband beamforming and source separation, in *Proceedings IEEE International Conference on Acoustics, Speech, and Signal Processing*, Vol. 3, 193–196.
- Langston, C. A. (2006). Spatial gradient analysis for linear seismic arrays, *Bull. Seism. Soc. Am.* (in press).
- Langston, C. A., P. Bodin, C. Powell, M. Withers, S. Horton, and W. Mooney (2005). Bulk sediment Qp and Qs in the Mississippi embayment, Central U.S., *Bull. Seism. Soc. Am.* **95**, 2162–2179.
- Miles, R. N., and S. Sundermuthy (2000). A biologically inspired direc-

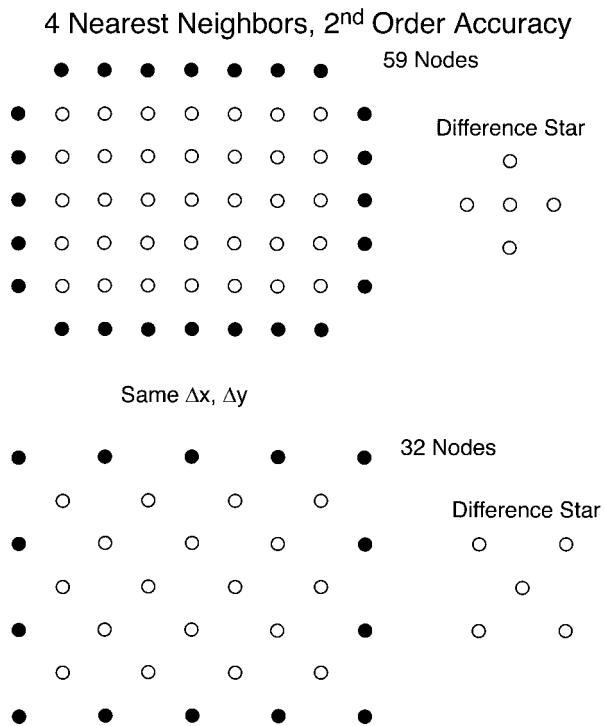


Figure 11. Two examples of large wave gradiometer arrays based on a lattice of finite-difference stars. There are four nearest neighbors in the finite-difference star, with the same Δx and Δy increments for both stars, and both have second-order accuracy. The top gradiometer array spacing is dense, but would be more expensive to deploy because of the increased numbers of instruments needed compared with the bottom gradiometer. The top gradiometer might be useful for structure studies within the confines of the array because of the instrument density. The bottom array may be more useful for nearby source studies.

tional microphone concept for hearing aids, Presented at *International Hearing Aid Research Conference*, Lake Tahoe, California.

Mooney, W. D., M. C. Andrews, A. Ginzburg, D. A. Peters, and R. M. Hamilton (1983). Crustal structure of the northern Mississippi embayment and a comparison with other continental rift zones, *Tectonophysics* **94**, 327–348.

Nawab, S., F. Dowlah, and R. Lacoss (1985). Direction determination of wideband signals, *IEEE Trans. Acoust. Speech Sig. Proc.* **33**, 1114–1122.

Robert, D., R. N. Miles, and R. R. Hoy (1999). Tympanal hearing in the saracophagid parasitoid fly *emblemiasoma* sp.: the biomechanics of directional hearing, *J. Exp. Bio.* **202**, 1865–1876.

Stanacevic, M., G. Cauwenberghs, and G. Zweig (2002). Gradient flow adaptive beamforming and signal separation in a miniature microphone array, in *Proceedings IEEE International Conference on Acoustics, Speech, and Signal Processing*, Vol. 4, 4016–4019.

Vogfjord, K. S., and C. A. Langston (1990). Analysis of regional events recorded at NORESS, *Bull. Seism. Soc. Am.* **80**, 2016–2031.

Wagner, G. S. (1997). Regional wave propagation in southern California and Nevada: observations from a three-component seismic array, *J. Geophys. Res.* **102**, 8285–8311.

Center for Earthquake Research and Information
University of Memphis
3876 Central Ave., Suite 1
Memphis, Tennessee 38152-3050

Manuscript received 23 June 2006.